Single-Phase Suspension Control of Bearingless Switched Reluctance Motor

Zhuliang Huang, *Graduate Student Member, IEEE*, Yi Hao, Xilian Wang, Xuan Wang, Wenmei Hao, Yan Su, and Ruikang Yang

***Abstract*—The article proposes a single-phase suspension control strategy with self-decoupling to address the complexity of decoupling control strategies caused by the coupling between radial suspension forces in two radial directions of bearingless switched reluctance motor (BSRM). The proposed single-phase control strategy aims to achieve stable rotor suspension by adjusting the current of the suspension winding only when one of the torque windings is excited instead of all torque wingdings. A sharing suspension windings bearingless switched reluctance motor (SSW-BSRM) is taken as research objective, the relationship between radial force and radial displacement of rotor with proposed single-phase suspension control strategy in one electrical cycle is analyzed. When the rotor speed exceeds a certain value, the feasibility of switching from three-phase suspension control to single-phase suspension control is theoretically analyzed. The expression of the critical speed of the rotor is derived, which reveals the speed requirement for achieving stable rotor suspension under the proposed single-phase suspension control strategy. The simulation and experiment are carried out on a 12/8 SSW-BSRM, and the results verify the effectiveness of the proposed single-phase control strategy in achieving stabilized rotor suspension with self-decoupling in two radial directions. Furthermore, the proposed control strategy can also be applied to the suspension control of conventional BSRMs.**

***Index Terms*—Bearingless switched reluctance motor (BSRM), critical speed, self-decoupling, sharing suspension windings, single-phase suspension.**

I. Introduction

BESSINGLESS switched reluctance motor (BSRM) inherits the advantages of simple structure, good speed regulation performance, robustness and durability of switched reluctance motor [1], [2], [3]. In addition, due to its compact size and inherent self-suspension and self-driving capabilities resulting from a stator winding structure similar to magnetic bearing winding, the BSRM holds considerable promise for applications in high-speed and ultra-high-speed flywheel energy storage, aerospace, and other drive scenarios [4], [5]. Dual-winding BSRM structure was the first to emerge and has been extensively studied [6], [7], [8]. In this structure, both torque and suspension windings are wound on the stator pole, and the air gap magnetic field is generated by both the torque winding and the suspension winding. Consequently, a strong coupling exists between motor torque and suspension force, posing challenges for achieving high-performance control of the BSRM.

Due to complex control problems caused by the coupling between torque and suspension forces of conventional BSRM structures, scholars have done related research on the motor structure and control strategies in order to improve the operation performance of the BSRM. In terms of motor structure improvement, a BSRM with 8/10 hybrid stator tooth structure was proposed [9], [10]. To realize the decoupling control of torque and suspension force, there are eight teeth on the stator of this topology, among which four stator poles are wound with torque winding and the other four poles are wound with suspension winding. However, the power density of this structure is low and the iron core loss is high. In order to solve the problems above, the structure of 12/14 hybrid stator pole BSRM [11], [12] and 12/8 double stator BSRM [13], [14] have been proposed. A permanent magnet-biased BSRM which consists of two motors and each motor has a 12/12 structure was presented in [15]. The permanent magnets between the two motors are used to provide bias flux for the radial force generation of this structure. To increase structure compactness, critical rotor speed, and output torque of structure presented in [15], an improved modular permanent magnet BSRM is comprehensively investigated [16]. The common feature of these three structures of motors is that the torque winding and the suspension winding are wrapped on different stator poles, respectively, which realizes the decoupling between suspension force and torque structurally, thus simplifying the control strategy.

In terms of decoupling control strategies, to achieve independent control of torque and suspension force, Cao et al. [17] proposed a control strategy that single and double phases conduct alternatively while the suspension winding current conducts in the fixed section. In [18], considering the influence of the change of rotor position on suspension control, a coupling suspension force regulator is designed to transform the suspension control system

Manuscript received 9 October 2023; revised 13 January 2024 and 5 March 2024; accepted 30 March 2024. Date of publication 10 April 2024; date of current version 16 May 2024. This work was supported by the Fundamental Research Funds for the Central Universities under Grant 2022JBZY015. Recommended for publication by Associate Editor A. M. Trzynadlowski. *(Corresponding author: Xilian Wang.)*

Zhuliang Huang, Xilian Wang, Xuan Wang, Yan Su, and Ruikang Yang are with the College of Electrical Engineering, Beijing Jiaotong University, Beijing 100044, China (e-mail: 22110439@bjtu.edu.cn; xlwang1@bjtu.edu.cn; 21121507@bjtu.edu.cn; 21121448@bjtu.edu.cn; 23115188@bjtu.edu.cn).

Yi Hao is with the Beijing Zongheng Electro-Mechanical Technology Company Ltd., Locomotive and Car Research Institute, China Academy of Railway Sciences Company Ltd., Beijing 100081, China (e-mail: 16117376@bjtu.edu.cn).

Wenmei Hao is with the National Engineering Research Center for Electric Vehicles and School of Mechanical Engineering, Beijing Institute of Technology, Beijing 100811, China (e-mail: haowenmei@bit.edu.cn).

This article has supplementary material provided by the authors and color versions of one or more figures available at https://doi.org/10.1109/TPEL.2024.3387091.

Digital Object Identifier 10.1109/TPEL.2024.3387091

from a time-varying system to a time-invariant steady system, which improves the robustness of the system. The inverse system method has been widely used in the decoupling control of motors in recent years. In [19], the support vector machine method was adopted to establish the BSRM inverse model, realizing the decoupling of BSRM torque and suspension force. However, only the decoupling issues of BSRM in the reversible domain were discussed in support vector machine methods. Since BSRM is an incomplete reversible system, the direct-inverse system and correctional-inverse system were employed in the reversible domain and irreversible domain, respectively, in [20] to realize the whole domain decoupling, which enhances the decoupling characteristics of the BSRM control system. However, the reversibility of the BSRM mathematical model is required to analyze for the inverse system method, so as to obtain the inverse model of BSRM, which causes inconvenience to the practical application by the complicated calculation process.

Radial suspension control of BSRM is realized by controlling two radial degrees of freedom, which are the *X*-direction (horizontal direction) and the *Y*-direction (vertical direction), respectively. For BSRM with conventional structure, coupling issues exist not only between torque and suspension force but also between suspension force in *X*-direction and the *Y*-direction. More specifically, the adjustment of suspension winding current in the *X*-direction will affect the suspension force in the *Y*-direction, and similarly, the adjustment of suspension winding current in the *Y*-direction will affect the suspension force in the *X*-direction. The coupling issues will further increase the complexity of BSRM suspension control, particularly at high speeds.

Therefore, a single-phase suspension control strategy with self-decoupling in the *X*-direction and *Y*-direction is proposed in the article. The suspension winding is controlled when only a specified phase torque winding is excited, addressing the coupling problem of BSRM between suspension force in the *X*-direction and *Y*-direction. In the article, an SSW-BSRM is taken as the research object, the suspension principle of SSW-BSRM and the principle of single-phase suspension control strategy are introduced. In addition, the critical speed required for rotor stable suspension in single-phase suspension control strategy is derived. A dynamic simulation model of SSW-BSRM with the single-phase suspension control is built in MATLAB/Simulink environment, and the feasibility of the single-phase suspension control strategy is simulated and analyzed. Finally, the experiment platform of SSW-BSRM with single-phase suspension control strategy is built to realize stable rotation and suspension of the rotor, and the validity of the proposed control strategy is verified. The main contributions of this article are as follows.

1) A single-phase suspension control strategy when only torque winding of phase B is excited is proposed to achieve the self-decoupling of suspension forces in both the *X*-direction and *Y*-direction of SSW-BSRM. Additionally, the proposed control strategy can also be applied to conventional BSRMs.
2) The critical speed for achieving stable rotor suspension under single-phase suspension control strategy is derived by establishing the second-order rotor kinematic equations based on the radial force model considering the rotor eccentricity.

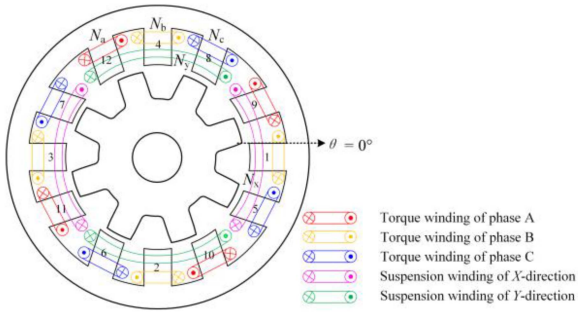

Fig. 1. Structure of the SSW-BSRM.

The rest of this article is organized as follows. In Section II the structure and the suspension principle of SSW-BSRM are introduced. In Section III, the critical speed to achieve stable rotor suspension during single-phase suspension is derived. In Section IV and Section V, to verify the effectiveness of the proposed single-phase suspension control strategy, simulation and experimental results are provided. Finally, Section VI concludes this article.

II. Control Principle of Single-Phase Suspension

A. SSW-BSRM

In this article, the SSW-BSRM is taken as the research object [21], [22], [23], and the structure of SSW-BSRM is shown in Fig. 1. Unlike the BSRM with conventional structure, the suspension windings of SSW-BSRM are stacked on three stator poles. The inductance of suspension winding varies little with rotor position, which means that the currents of suspension winding have little effect on the torque. The key advantage of this structure is the structural decoupling characteristic of the motor torque and suspension force. Rotation control of SSW-BSRM is similar to the switched reluctance motors, and the radial suspension is realized by controlling the value and direction of suspension winding currents in the *X*-direction and *Y*-direction. In the radial suspension control of the conventional dual-winding BSRM, the suspension winding current needs to be switched according to the torque winding. But for SSW-BSRM, the suspension winding currents do not need to be switched with the switching of the torque winding during rotor rotation operation, and only the value and direction of the suspension winding currents are needed to determine according to the rotor eccentric position signals. The winding structure of the motor is simple. Regardless of the number of motor phases, only two sets of suspension windings are needed to realize rotor radial suspension control. Because it is not necessary to switch suspension windings during operation, the control circuit and control algorithm are simplified.

B. Principle of Single-Phase Suspension

Fig. 2 shows the magnetic flux scheme and the distribution of suspension force of SSW-BSRM when torque winding of phases

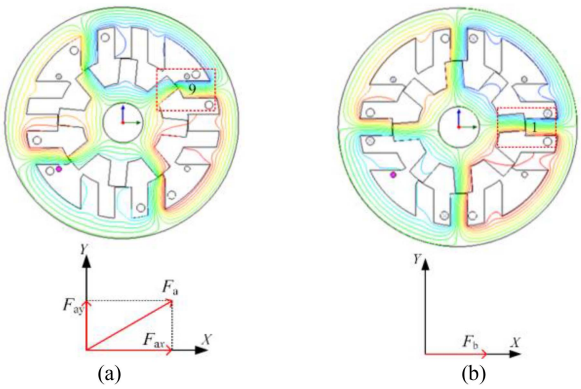

Fig. 2. Scheme of magnetic flux and suspension force. (a) Phase A is excited. (b) Phase B is excited.

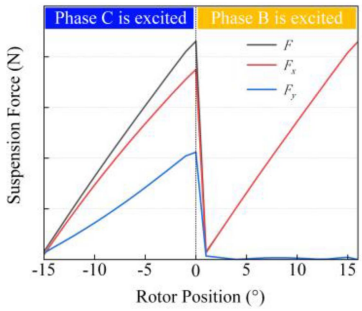

Fig. 3. Variation of suspension force as the rotor position changes.

A and B are excited, respectively. The position of phases A, B, and C phase in SSW-BSRM are shown in Fig. 1, where phase B is located in horizontal and vertical directions. As shown in Fig. 2(a), when suspension winding in the *X*-direction is adjusted during phase A is excited, the suspension force generated at pole 9 can be decomposed into force components in both the *X*-direction and *Y*-direction, which are F_{ax} and F_{ay}, respectively. Therefore, the adjustment of the suspension winding current in the *X*-direction will cause displacement of the rotor in both the *X*-direction and *Y*-direction. Same phenomenon occurs when the suspension winding current in the *Y*-direction is excited. That is, during the excitation of phase A, the coupling effect appears in the *X*-direction and *Y*-direction with suspension control. However, as shown in Fig. 2(b), when phase B is excited, the suspension force F_b generated by the adjustment of the suspension winding current in the *X*-direction is significantly greater than that in the *Y*-direction. Therefore, the suspension force in the *Y*-direction can be ignored in this situation. This means that adjusting the suspension winding current in the *X*-direction during the excitation of phase B will only cause displacement of the rotor in the *X*-direction, but not in the *Y*-direction. And it is the same for the *Y*-direction. The situation of phase C is similar to phase A. Fig. 3 shows the variation of suspension force as the rotor position changes. It can be seen that when phase C is excited, the suspension force can be decomposed into two components. However, this phenomenon does not occur during phase B is excited. Therefore, if the suspension winding currents in the *X*-direction and *Y*-direction are adjusted only when phase B is excited, the displacement in the *X*-direction and *Y*-direction can be controlled independently. The self-decoupling of the suspension control in *X*-direction and *Y*-direction is realized.

III. Calculation and Analysis of the Critical Speed

The single-phase suspension control strategy proposed in this article is implemented when only the torque winding of phase B is excited. Although the suspension winding is not conducted when the phase A and phase C are excited, the rotor will also be subjected to the radial force produced by phase A or phase C as long as there is eccentricity on the rotor. During a whole electrical cycle, the rotor is controlled only when the phase B is excited, and is not controlled when phase A and phase C are excited. Therefore, in order to ensure stable suspension of the rotor without collision with the auxiliary backup bearing, the rotor speed must be higher than a critical value, which is called critical speed in the following. The radial force and radial displacement when the phase A, phase B, and phase C are excited will be calculated, respectively. And then critical speed can be obtained by kinematic equation of rotor.

A. Analysis of Suspension Force and Radial Displacement With the Proposed Control Strategy

According to the derivation in [22], the radial force expression of the SSW-BSRM considering the rotor eccentricity can be expressed as

$$\begin{cases} F_x = 8N_m^2 i_m^2 \mu_0 hr \cdot \frac{g_0\theta\alpha(\theta^2+1)}{(2{g_0}^2-\alpha^2(\theta^2+1))^2} \\ \qquad + 4N_m i_m N_x i_x \mu_0 hr \cdot \frac{2g_0^2\theta+\alpha^2\theta^3+\alpha^2\theta}{(2{g_0}^2-\alpha^2(\theta^2+1))^2} \\ F_y = 8N_m^2 i_m^2 \mu_0 hr \cdot \frac{g_0\theta\beta(\theta^2+1)}{(2{g_0}^2-\beta^2(\theta^2+1))^2} \\ \qquad + 4N_m i_m N_y i_y \mu_0 hr \cdot \frac{2g_0^2\theta+\beta^2\theta^3+\beta^2\theta}{(2{g_0}^2-\beta^2(\theta^2+1))^2} \end{cases} \tag{1}$$

where N_m is the number of turns of the torque winding; N_x and N_y are the number of turns of the suspension winding in the *X*-direction and *Y*-direction, respectively; i_m is the current of the torque winding; i_x and i_y are the current of the suspension winding in the *X*-direction and *Y*-direction, respectively; α and β are the radial displacements of the rotor in the *X*-direction and *Y*-direction, respectively; θ is the rotor position; μ_0 is the vacuum permeability; h is axial length of the rotor; r is the outside diameter of the rotor; g_0 is the length of the air gap; Since the structure is symmetric in the *X*-direction and *Y*-direction, the *X*-direction is taken as an example for the following analysis in this article.

When phase B is excited, the radial force in the *X*-direction is expressed as (1). As $\theta^2 \ll 1$, it can be treated as $\theta^2 + 1 \approx 1$, and the condition $2g_0^2 - \alpha^2 > g_0^2$ holds as $\alpha < g_0$. Therefore, when phase B is excited, the radial force in the X-direction can be simplified as

$$F_{xb} < \frac{4\mu_0 hr\theta}{g_0^2}\left(2N_{mb}^2 i_{mb}^2 + 3N_{mb} i_{mb} N_x i_x\right). \tag{2}$$

When phase A is excited, according to the position of rotor shown in Fig. 2(a). The suspension winding is not conducted,

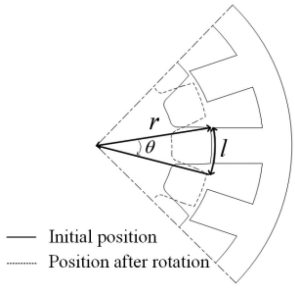

Fig. 4. Arc length diagram of rotor rotation.

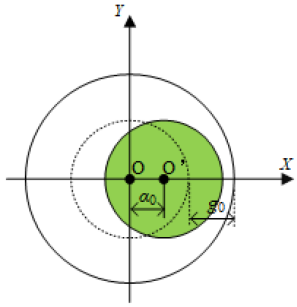

Fig. 5. Schematic diagram of rotor eccentricity.

and the radial force in the *X*-direction can be written as

$$F_{xa} = 8N_{ma}^2 i_{ma}^2 \mu_0 hr\theta g_0 \frac{\alpha(\theta^2+1)}{\left[2g_0^2 - \alpha^2(\theta^2+1)\right]^2} \cdot \cos 30^\circ - 8N_{ma}^2 i_{ma}^2 \mu_0 hr\theta g_0 \frac{\beta(\theta^2+1)}{\left[2g_0^2 - \beta^2(\theta^2+1)\right]^2} \cdot \sin 30^\circ. \tag{3}$$

In order to simplify the calculation process, the influence caused by the displacement of the rotor in the *Y*-direction on the force in the *X*-direction is ignored. Therefore, set $\beta = 0$, and with the conditions $\theta^2 + 1 \approx 1$ and $2g_0^2 - \alpha^2 > g_0^2$, (3) can be further simplified as

$$F_{xa} < \frac{4\sqrt{3}\mu_0 hr\theta}{g_0^2} N_{ma}^2 i_{ma}^2. \tag{4}$$

Similarly, when phase C is excited, the force in the *X*-direction will meet the following condition:

$$F_{xc} < \frac{4\sqrt{3}\mu_0 hr\theta}{g_0^2} N_{mc}^2 i_{mc}^2. \tag{5}$$

In Fig. 4, the solid line shows the initial position of the rotor, and the dotted line shows the rotor position when the rotor rotates θ rad. The arc length l with rotor turning θ rad can be expressed as

$$l = r\theta. \tag{6}$$

Thus, the time required for the rotor to turn the arc length l can be expressed as

$$t = \frac{l}{\omega} = \frac{30\theta}{\pi n} \tag{7}$$

where ω is the angular speed and the n is the rotation speed of the rotor.

Take derivative of both sides of (7)

$$dt = \frac{30}{\pi n} d\theta. \tag{8}$$

According to the rotor kinematic equation, the rotor displacement with phase B excited is the double integrals of the rotor radial force over time, which can be expressed as

$$\alpha_b = \int\int \frac{F_{xb}}{m} dtdt. \tag{9}$$

Substitute (2) and (8) into (9) yields

$$\alpha_b < \frac{25\mu_0 h\pi r}{72mn^2 g_0^2} \left(2N_{mb}^2 i_{mb}^2 + 3N_{mb} i_{mb} N_x i_x\right). \tag{10}$$

Similarly, the radial displacement of the rotor with phase A and phase C excited can be obtained as

$$\alpha_a < \frac{25\mu_0 h\pi r}{72mn^2 g_0^2} \cdot \sqrt{3} N_{ma}^2 i_{ma}^2 \tag{11}$$

$$\alpha_c < \frac{25\mu_0 h\pi r}{72mn^2 g_0^2} \cdot \sqrt{3} N_{mc}^2 i_{mc}^2. \tag{12}$$

The condition of the radial displacement in the *X*-direction can be reached by adding the three radial displacements expressed in conditions (10), (11), and (12) together as

$$\alpha = \alpha_a + \alpha_b + \alpha_c < \frac{25\mu_0 h\pi r}{72mn^2 g_0^2} \cdot \left(\sqrt{3} N_{ma}^2 i_{ma}^2 + 3N_{mb} i_{mb} N_x i_x + 2N_{mb}^2 i_{mb}^2 + \sqrt{3} N_{mc}^2 i_{mc}^2\right). \tag{13}$$

Therefore, the maximum radial displacement in the *X*-direction in one electrical cycle is given by

$$\alpha_{\max} = \frac{25\mu_0 h\pi r}{72mn^2 g_0^2} \cdot \left(\sqrt{3} N_{ma}^2 i_{ma}^2 + 3N_{mb} i_{mb} N_x i_x + 2N_{mb}^2 i_{mb}^2 + \sqrt{3} N_{mc}^2 i_{mc}^2\right). \tag{14}$$

B. Analysis of Critical Speed

Fig. 5 shows the eccentricity of the rotor, *O* is the geometric center of the motor and *O*' is the center of the rotating shaft. Assuming that the initial eccentricity displacement in the *X*-direction is α_0, it can be seen from Fig. 5 that the range of the rotor movement in the positive direction of *X* axis is

$$0 < \alpha < g_0 - \alpha_0. \tag{15}$$

The range of the rotor movement in the negative direction of the *X*-axis is

$$0 < \alpha < g_0 + \alpha_0. \tag{16}$$

Since the movement range of the rotor are not the same on the two sides, the smaller side of the movement range should be

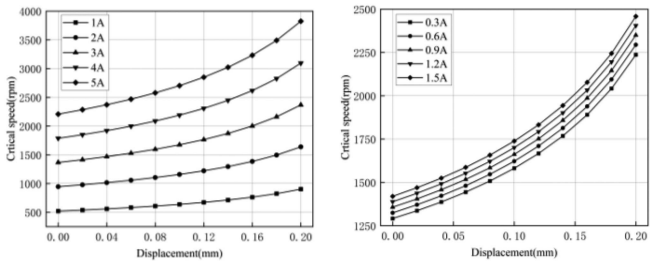

(a) (b)

Fig. 6. Relationship among critical speed and displacement, torque winding current and suspension winding current. (a) Change of torque winding current. (b) Change of suspension winding current.

TABLE I
STRUCTURE PARAMETERS OF THE PROTOTYPE

Parameters	Value
Number of stator poles	12
Number of rotor poles	8
Number of torque winding turns	23
Number of suspension winding turns	23
Rated voltage	50 V
Rated current	4.25 A
Rated speed	8500 r/min
Rated torque	0.155 N·m
Outer diameter of the stator	110 mm
Inner diameter of the stator	67 mm
Outer diameter of the rotor	66.4 mm
Axial length of the rotor	62 mm
Air gap between stator and rotor	0.3 mm
Air gap between shaft and backup bearing	0.2 mm

taken into consideration in the calculation process of the critical speed. Therefore, the critical speed condition can be obtained by substituting (15) into (13)

Similarly, (17) shown at the bottom of this page, can be deduced by applying radial force in *Y*-direction expressed in (1).

In addition, it is necessary to take the geometrical condition of the shaft movement into consideration.

$$\alpha^2 + \beta^2 < g_0^2. \tag{18}$$

To illustrate the relationship among the critical speed, the radial displacement in the *X*-direction, the torque winding currents, and the suspension winding currents, the curves based on (17) are shown in Fig. 6 with the motor structure parameters given in Table I. In Fig. 6(a), the suspension winding currents in the *X*-direction and *Y*-direction are 1 and 0 A, respectively, and the torque winding currents are 1, 2, 3, 4, and 5 A, respectively.

Fig. 6(b) shows the curves with the torque winding current of 3 A and *Y*-direction suspension winding current of 0 A, while the suspension winding currents in *X*-direction are 0.3, 0.6, 0.9, 1.2, and 1.5 A, respectively. The critical speed increases with the increase of the radial displacement and also with the increase of torque winding current and suspension winding current.

It should be noted that the process of deriving the critical speed expression in this article has been approximated. It means that the single-phase suspension control strategy can be achieved as long as the speed is greater than the calculated value, and it is possible to achieve if the speed is lower than this value.

IV. SIMULATION ANALYSIS OF SINGLE-PHASE SUSPENSION CONTROL STRATEGY

A. Analysis of Suspension Force and Radial Displacement With the Proposed Control Strategy

In order to verify the feasibility of the control strategy proposed in this article, the control block of single-phase suspension control system of SSW-BSRM is built in MATLAB/Simulink environment as shown in Fig. 7, in which the motor model is obtained by finite-element modeling (FEM) simulation based on the motor structure parameters given in Table I, and the FEM results are stored in the form of the table. "Speed-current" and "displacement-current" double closed-loop control strategies are adopted for controlling the speed and the radial displacement, respectively. n^* is the given speed, α^* and β^* are the given displacements in the *X*-direction and *Y*-direction, respectively. The PI controllers are adopted for the "speed-current" double closed-loop. The outputs of the PI controller are the reference currents of torque winding i^*. The PD controllers are adopted for the "displacement-current" double closed-loop. The outputs of the PD controller are the reference currents of suspension winding $i_x{}^*$ and $i_y{}^*$. The hysteresis controllers are used as the current controller to regulate the torque winding current and suspension winding current in the inner loop. In the simulation, the minimum simulation step size is set to 40 μs. Hence, the maximum control frequency is 25 kHz. Meanwhile, the critical speed of the motor is calculated by the single-phase suspension controller. As long as the motor speed is higher than the calculated critical speed, the single-phase suspension control signal will be applied to the suspension winding current controller to switch the control system to the single-phase suspension control mode.

B. Simulation of Proposed Control Strategy

In the simulation model, the initial eccentric displacement of the rotor is set to 0.15 mm and the air gap length is 0.3 mm. To be consistent with the following experiment, the backup bearing is set up in simulation, and the rotor is movable in the range of -0.2 to 0.2 mm. The motor is started with the three-phase suspension control strategy, and the given speed is 3200 r/min. When the motor speed is greater than the critical speed determined by (17), the system is switched from three-phase suspension control mode to single-phase suspension control mode. During the single-phase suspension mode, a 5 N radial disturbance with a duration of 0.02 s in the *X*-direction is applied to the rotor at 4 s to verify the anti-interference ability of the system.

$$n > \sqrt{\frac{25\mu_0 h\pi r}{72m\left(g_0-\alpha_0\right)g_0^2}\left(\sqrt{3}N_{ma}^2 i_{ma}^2 + 3N_{mb}i_{mb}N_x i_x + 2N_{mb}^2 i_{mb}^2 + \sqrt{3}N_{mc}^2 i_{mc}^2\right)}. \tag{17}$$

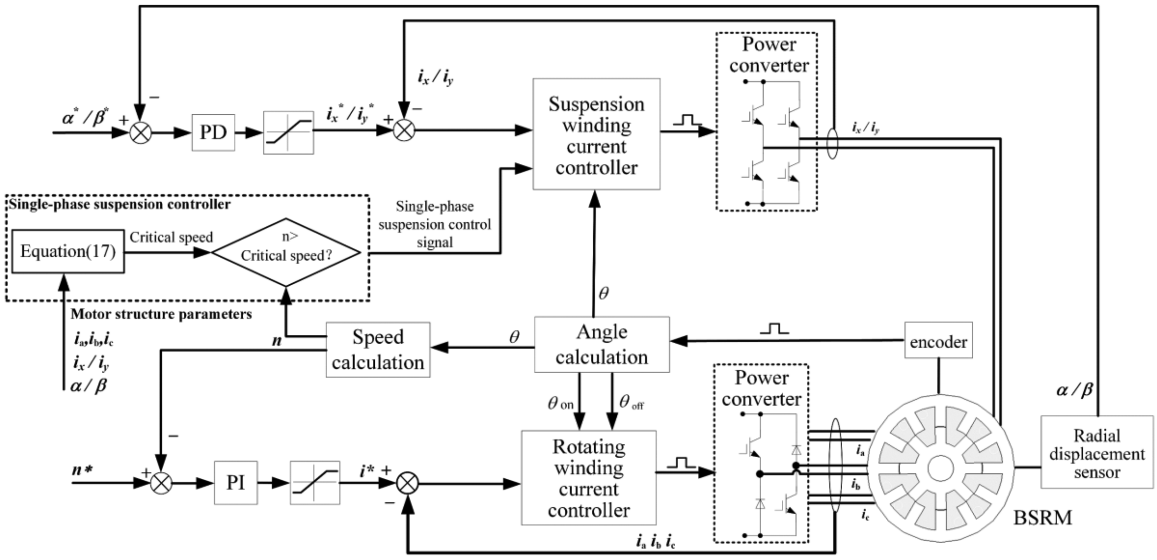

Fig. 7. Control block of proposed control strategy.

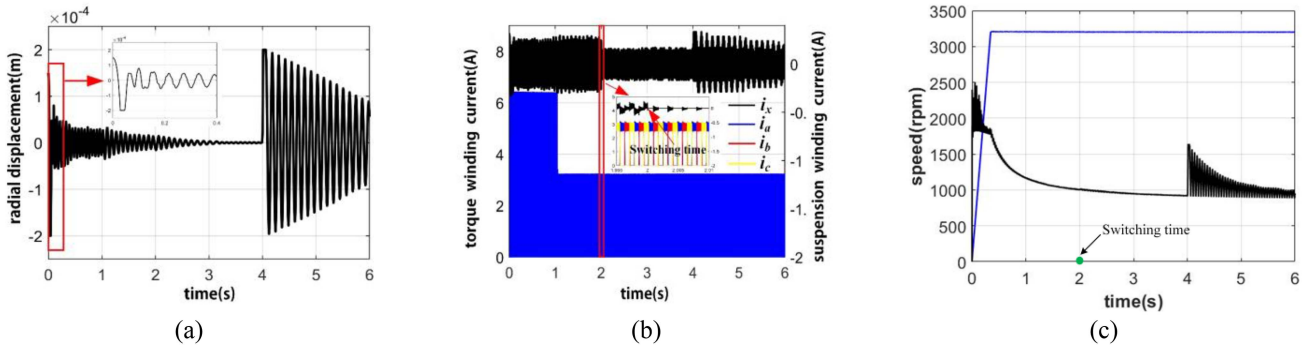

(a) (b) (c)

Fig. 8. Simulation results of switching to proposed control strategy over critical speed. (a) Radial displacement in *X*-direction. (b) Torque winding current and suspension winding currents. (c) Speed and critical speed.

Fig. 8 shows the radial displacement curve in the *X*-direction, the currents curve of each winding, and the speed curve of the motor. From Fig. 8(a)–(c), it can be seen that the rotor is suspended stably after switching from three-phase to single-phase suspension mode, and the rotor speed is not affected. After the radial disturbance in the *X*-direction is applied to the rotor which operates under single-phase suspension control strategy, the radial displacement in the *X*-direction increases instantaneously and then decreases gradually. Still the rotor is suspended stably and the speed is not affected. Fig. 8(b) shows the curves of torque and suspension winding currents. It can be seen that the suspension winding is intermittently conducted, and the conducting time is the same as that of phase B. After radial disturbance in the *X*-direction is applied to the rotor at 4 s, the suspension winding current in the *X*-direction increases simultaneously in order to overcome the disturbance, and then gradually decreases with the decrease of radial displacement. The rotor touches the backup bearing only during the period of the start-up and the application of radial disturbance, and the rotor are controlled within the range of −0.2 to 0.2 mm in the other period of the whole dynamic process. Especially when the three-phase suspension control strategy is switched to the proposed control strategy and when the disturbance is applied under the single-phase suspension control strategy, the system can also remain stable. The validity of the single-phase suspension control strategy proposed is verified by the simulation.

C. Simulation of Switching to the Proposed Control Strategy Below the Critical Speed

Fig. 9 shows the simulation results of the system when the system switches to the single-phase suspension control strategy with the speed lower than the critical speed. At 0.02 s, the system switches to the single-phase suspension control strategy, while the motor speed is lower than the critical speed calculated by (17). It can be seen from Fig. 9(a) that the rotor touches the backup bearing (±0.2 mm) several times after switching mode. Although with the speed increasing, the rotor can gradually tend to be stable suspension. However, compared with Fig. 8(a), the

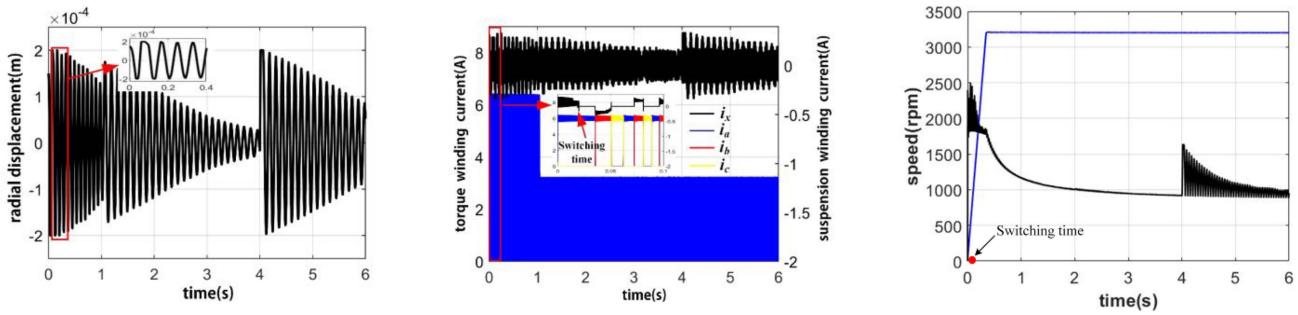

(a) (b) (c)

Fig. 9. Simulation results of switching to proposed control strategy below critical speed. (a) Radial displacement in *X*-direction. (b) Torque winding currents and suspension winding currents. (c) Speed and critical speed.

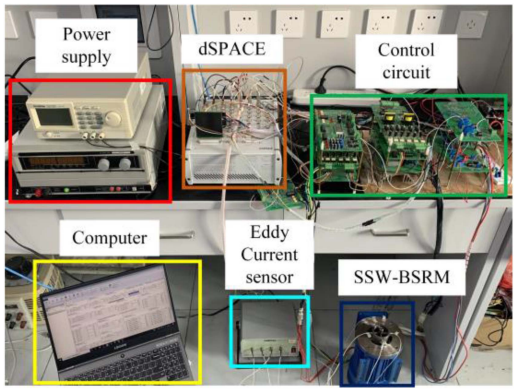

Fig. 10. Experimental platform.

suspension effect of the rotor is poorer after the mode is switched with the speed lower than the critical speed.

V. Experimental Verification

In this section, the proposed single-phase suspension control strategy is validated by experiments on a 0.137 kW three-phase 12/8 SSW-BSRM test bench, as shown in Fig. 10. The parameters of the prototype are given in Table I. The control circuit is composed of a three-phase asymmetric half-bridge power converter dedicated to the torque winding, a full-bridge power converter dedicated to the suspension winding, and the sampling circuits for detecting the winding currents, rotor position, and rotor radial displacement. The proposed single-phase suspension control algorithm is implemented in a dSPACE-DS1202 platform at the maximum sampling frequency of 50 kHz. The power supply for the torque winding is ZWY30010 which can provide 300 V and 10 A, and the power supply for the torque winding is PSP-603 which can provide 60 V and 3.5 A. The position of the rotor is sampled by photoelectric sensors. The displacements of the shaft at the direction of *X*-direction and *Y*-direction are measured by the eddy current sensor. To avoid the collision between the stator and rotor when the SSW-BSRM operates, an auxiliary backup bearing is installed. The radial distance between the shaft and the inner ring of auxiliary backup bearing is 0.2 mm, while the length of air-gap between stator and rotor is 0.3 mm.

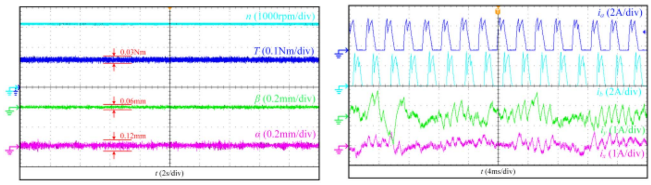

(a) (b)

Fig. 11. Experimental results of three-phase suspension control mode. (a) Speed, torque, displacements in the *X*-direction and *Y*-direction. (b) Torque winding currents of phases A and B, suspension winding current in the *X*-direction and *Y*-direction.

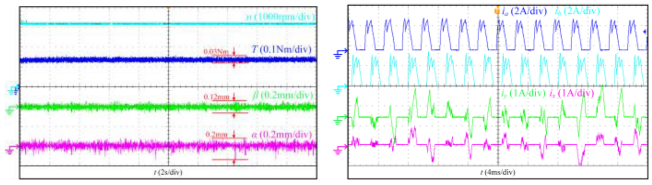

(a) (b)

Fig. 12. Experimental results of single-phase suspension control mode. (a) Speed, torque, displacements in the *X*-direction and *Y*-direction. (b) Torque winding currents of phases A and B, suspension winding current in the *X*-direction and *Y*-direction.

A. Steady Performance of Three-Phase Suspension Control and Single-Phase Suspension Control

Figs. 11 and 12 show the experimental results of speed, torque, radial displacements in the *X*-direction and *Y*-direction, and torque winding current at the speed of 3200 r/min when the SSW-BSRM operates in the three-phase suspension mode and single-phase suspension mode, respectively. As shown in Fig. 11, the currents of suspension winding are controlled continuously regardless of the conduction of torque winding in three-phase suspension mode, and the radial displacements α and β of the shaft in the *X*-direction and *Y*-direction are both controlled within ± 0.12 mm. It can be seen from Fig. 12 that the currents of suspension winding are intermittently excited in the single-phase suspension mode, and the excitation time is consistent with that of the torque winding of phase B. The radial displacement in the *X*-direction and *Y*-direction are both

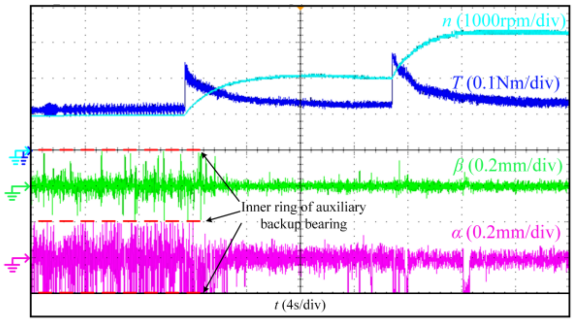

Fig. 13. Experimental result in a variable speed condition.

controlled within ±0.2 mm. The radial displacements in two operating modes are both smaller than the clearance between the shaft and the inner ring of the backup bearing. According to [18], the inductance of suspension winding varies little with rotor position, which means that the currents of suspension winding have little effect on the torque. Consequently, there is no significant difference in torque between two operating modes.

B. Dynamic Performance of Single-Phase Suspension Control

In order to test the performance in variable speed conditions, a dynamic test for the proposed single-phase suspension control strategy is illustrated in Fig. 13. The motor is initially controlled to 1000 r/min, and then the speed is increased to 2000 r/min and then increased to 3200 r/min. It can be seen that the motor torque increases during the process of speed increase, and the motor torque returns to stability when the speed reaches the given speed. Under the single-phase suspension control strategy, the rotor is not able to be suspended stably at 1000 r/min because the speed is lower than the critical speed calculated in (17). As the speed increases, the suspension stability of the rotor improves under the single-phase suspension control strategy.

C. Switching Process of Two Operating Modes

Fig. 14 shows the experiment results of switching process from three-phase suspension mode to single-phase suspension mode under 3200 and 1000 r/min, respectively. From Fig. 14(a), the motor is switching from three-phase to single-phase suspension control at the speed of 3200 r/min, which is higher than the critical speed calculated by (17). It can be seen that after the motor is switched to single-phase suspension control mode, although the suspension effect is not as good as that of three-phase mode, the rotor can still maintain stable suspension. The radial displacement in the X-direction and Y-direction are both controlled within ±0.2 mm. Fig. 14(b) shows the switching process at the speed of 1000 r/min, which is lower than the critical speed calculated by (17). It can be seen that after the motor is switched to single-phase suspension control mode, the rotor cannot maintain stable suspension in single-phase suspension mode. The shaft is in constant contact with the inner ring of the auxiliary backup bearing.

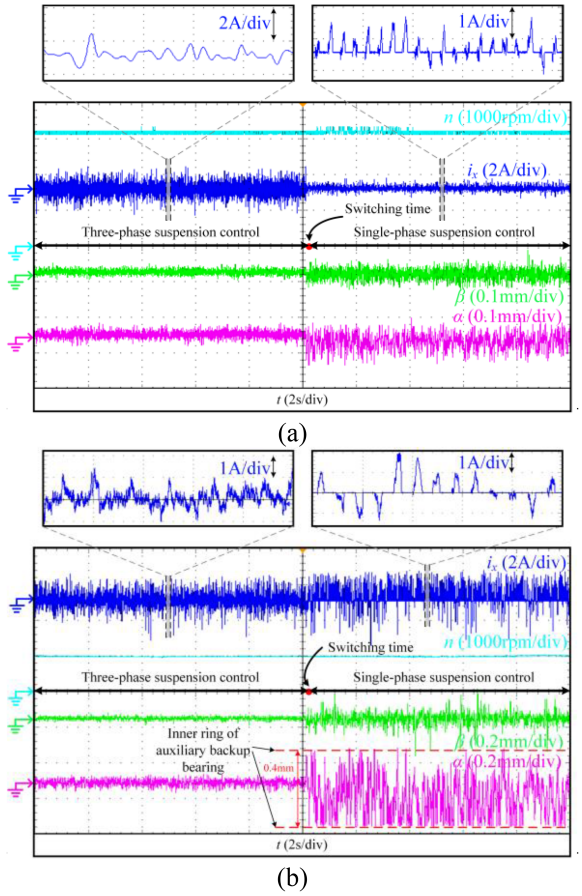

Fig. 14. Experimental results of switching from three-phase suspension mode to single-phase suspension mode. (a) 3200 r/min. (b) 1000 r/min.

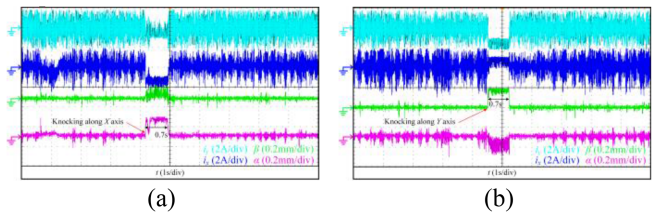

Fig. 15. Experimental results of knocking under three-phase suspension control. (a) Knocking along X-axis. (b) Knocking along Y-axis.

D. Self-Decoupling Characteristics of Single-Phase Suspension Control

To test the self-decoupling characteristics of the proposed control strategy, experiments with knocking on the shaft were implemented. Fig. 15 illustrates the experimental results of knocking shaft under three-phase suspension mode. In Fig. 15(a), a knocking with 0.7 s along the X-axis is applied to the shaft. It can be seen that the suspension winding current in the X-direction is adjusted to make the rotor return to the center position. However, during the adjustment process of the X-direction, the shaft deviates away from the center position both in the X-direction and Y-direction when an external force along X-axis applies to the shaft. Fig. 14(b) illustrates the experimental

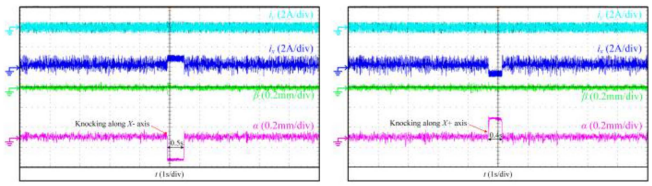

Fig. 16. Experimental results of knocking along X-axis under single-phase suspension control. (a) Knocking along X- axis. (b) Knocking along $X+$ axis.

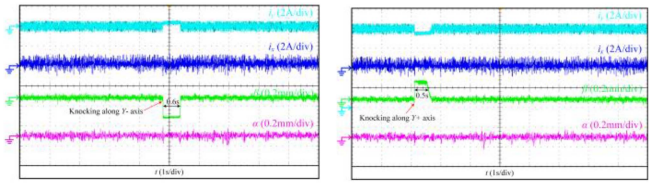

Fig. 17. Experimental results of knocking along Y-axis under single-phase suspension control. (a) Knocking along Y- axis. (b) Knocking along $Y+$ axis.

results of the knocking along the Y-axis. Similar to knocking along the X-axis, the adjustment of the suspension current in the Y-direction results in radial displacements of both the X-direction and Y-direction. The experimental results demonstrate that there is a coupling issue between the suspension forces in the two radial directions.

Figs. 16 and 17 illustrate the experimental results of knocking shaft under single-phase suspension mode. Fig. 16 shows the experimental results of knocking along X-axis under single-phase suspension control. It can be seen that the suspension winding current in the X-direction is adjusted once the disturbance is applied on the shaft along the X-axis. During the adjustment process of the X-direction, there is no radial displacement in Y-direction regardless of knocking along the $X+$ axis or X-axis. Fig. 17 shows the experimental results of knocking along the X-axis under single-phase suspension control. There is no radial displacement in the X-direction regardless of knocking along the $Y+$ axis or the Y- axis during the adjustment of the current of suspension winding in the Y-direction. Compared to the three-phase suspension control mode, the experimental results of the single-phase suspension can realize the decoupling of suspension force between the X-direction and Y-direction.

VI. Conclusion

In this article, a single-phase suspension control strategy where adjusting the currents of suspension winding when only torque winding of phase B is excited is proposed to realize the self-decoupling of suspension forces in the X-direction and Y-direction of SSW-BSRM. The proposed single-phase suspension control strategy in the article assumes a prerequisite, requiring the motor speed to exceed the critical speed. The critical speed to achieve stable rotor suspension during single-phase suspension control strategy is derived by establishing the second-order rotor kinematic equations based on the radial force model considering the rotor eccentricity. The control strategy proposed in this article has considerable generality and can be fully applied to bearingless switched reluctance motors with the general structure to achieve decoupled control of the suspension force in X-direction and Y-direction. In addition, the simplified control algorithm results in shorter program execution times, which makes that single-phase suspension control mode more conducive to high-speed operation compared with three-phase suspension control mode. The results of the simulation and experiment validate that the proposed control strategy can realize the decoupling of the suspension force in two radial directions. The proposed single-phase suspension control strategy provides the possibility and theoretical basis for designing new structure BSRM with higher compactness.

References

[1] R. Banerjee and P. Sensarma, "Digital peak current program mode controller for switched reluctance machines," *IEEE Trans. Power. Electron.*, vol. 38, no. 4, pp. 5230–5239, Apr. 2023.

[2] X. Guo, S. Zeng, M. Wu, R. Zhong, and W. Hua, "A direct drive sensorless starting scheme based on triple current threshold method in switched reluctance machines for low-cost current sampling applications," *IEEE Trans. Power. Electron.*, vol. 38, no. 7, pp. 8730–8741, Jul. 2023.

[3] C. Gan, J. Wu, Y. Hu, S. Yang, W. Cao, and J. M. Guerrero, "New integrated multilevel converter for switched reluctance motor drives in plug-in hybrid electric vehicles with flexible energy conversion," *IEEE Trans. Power. Electron.*, vol. 32, no. 5, pp. 3754–3766, May 2017.

[4] T. Zhu, X. Cao, Q. Yu, Z. Deng, and Z. Hao, "Direct torque control with phase commutation optimization for single-winding bearingless switched reluctance motor," *IEEE Trans. Power. Electron.*, vol. 37, no. 11, pp. 13238–13249, Nov. 2022.

[5] Z. Zhu, J. Wang, and M. Cheng, "A novel axial split phase bearingless flywheel machine with hybrid-inner-stator permanent magnet-based structure," *IEEE Trans. Power. Electron.*, vol. 36, no. 3, pp. 1873–1882, Sep. 2021.

[6] M. Takemoto, A. Chiba, H. Akagi, and T. Fukao, "Radial force and torque of a bearingless switched reluctance motor operating in a region of magnetic saturation," *IEEE Trans. Ind. Appl.*, vol. 40, no. 1, pp. 103–112, Feb. 2004.

[7] X. Cao, Q. Sun, C. Liu, H. Zhou, and Z. Deng, "Direct control of torque and levitation force for dual-winding bearingless switched reluctance motor," *Elect. Power Syst. Res.*, vol. 145, no. 1, pp. 214–222, Apr. 2017.

[8] X. Wang, Q. Tan, X. Liu, and B. Ge, "Improved radial force modeling and rotor suspension dynamics simulation studies for double-winding bearingless switched reluctance motor," *Elect. Power Compon. Syst.*, vol. 45, no. 1, pp. 111–120, Nov. 2017.

[9] H. Wang, Y. Wang, X. Liu, and J.-W. Ahn, "Design of novel bearingless switched reluctance motor," *IET Elect. Power Appl.*, vol. 6, no. 2, pp. 73–81, Feb. 2012.

[10] Y. He, Y. Tang, D.-H. Lee, and J.-W. Ahn, "Suspending control scheme of 8/10 bearingless SRM based on adaptive fuzzy PID controller," *Chin. J. Elect. Eng.*, vol. 2, no. 2, pp. 60–67, Dec. 2016.

[11] Z. Xu and F. Zhang, and J. -W. Ahn, "Design and analysis of a novel 12/14 hybrid pole type bearingless switched reluctance motor," in *Proc. IEEE Int. Symp. Ind. Electron.*, 2012, pp. 1922–1927.

[12] H. Wang, B. Xue, and S. Tang, "New type 12/14 bearingless switched reluctance motor with double windings," *IET Elect. Power Appl.*, vol. 9, no. 7, pp. 478–485, Aug. 2015.

[13] W. Peng, D.-H. Lee, F. Zhang, and J.-W. Ahn, "Design and characteristic analysis of a novel bearingless SRM with double stator," in *Proc. Int. Conf. Elect. Mach. Syst.*, 2011, pp. 1–6.

[14] Z. Xu, D.-H. Lee, and J.-W. Ahn, "Comparative analysis of bearingless switched reluctance motors with decoupled suspending force control," *IEEE Trans. Ind. Appl.*, vol. 51, no. 1, pp. 733–734, Feb. 2015.

[15] H. Wang and F. Li, "Design consideration and characteristic investigation of modular permanent magnet bearingless switched reluctance motor," *IEEE Trans. Ind. Electron.*, vol. 67, no. 6, pp. 4326–4337, Jun. 2020.

[16] H. Wang, J. Liu, J. Bao, and B. Xue, "A novel bearingless switched reluctance motor with a biased permanent magnet," *IEEE Trans. Ind. Electron.*, vol. 61, no. 12, pp. 6947–6955, Dec. 2014.

[17] X. Cao, Z. Deng, G. Yang, and X. Wang, "Independent control of average torque and radial force in bearingless switched-reluctance motors with hybrid excitations," *IEEE Trans. Power Electron.*, vol. 24, no. 5, pp. 1376–1385, May 2009.
[18] F. Yang, Y. Yuan, Y. Sun, S. Ding, L. Yan, and J. Xu, "Coupling suspension force regulator considering time-varying characteristic for a bearingless switched reluctance motor," *IEEE Trans. Ind. Electron.*, vol. 70, no. 7, pp. 6632–6641, Jul. 2023.
[19] K. Yang, Z. Zhu, and Y. Sun, "Decoupling control of single winding bearingless switched reluctance motors based on support vector machine inverse system," in *Proc. Int. Conf. Electr. Mach. Syst.*, 2014, pp. 1829–1833.
[20] Z. Zhu, Y. Sun, and Y. Yuan, "Decoupling control for dual-winding bearingless switched reluctance motor based on improved inverse system method," *Math. Probl. Eng.*, vol. 2017, 2017, Art. no. 5853423.
[21] R. Cui, Y. Hao, X. Wang, X. Fang, and Z. Huang, "Torque analytical model and self decoupling characteristics analysis of a bearingless switched reluctance motor," *IET Power Electron.*, vol. 14, no. 6, pp. 1149–1156, May 2021.
[22] X. Wang, B. Ge, J. Wang, and F. J. Ferreira, "Radial force analytic modeling for a novel bearingless switched reluctance motor when considering rotor eccentricity," *Elect. Power Compon. Syst.*, vol. 42, no. 6, pp. 544–553, Mar. 2014.
[23] Z. Huang, X. Wang, X. Wang, and L. Che, "A DITC method with copper loss minimum during commutation region of bearingless switched reluctance motor," in *Proc. IEEE 6th Student Conf. Elect. Mach. Syst.*, 2023, pp. 1–8.

Zhuliang Huang (Graduate Student Member, IEEE) received the B.S. degree in electrical engineering from Shanghai Maritime University, Shanghai, China, in 2020. He is currently working toward the Ph.D. degree in electrical engineering with the Beijing Jiaotong University, Beijing, China.

His research interests include bearingless switched reluctance motors.

Yi Hao received the B.S. degree in automation from Wuhan University of Science and Technology, Wuhan, China, in 2012, M.S. degree in electrical engineering from Illinois Institute of Technology, U.S., in 2015, and the Ph.D. degree in electrical engineering from Beijing Jiaotong University, China, in 2022.

He is currently a Research Assistant wiyj Beijing Zongheng Electro-Mechanical Technology Company Ltd., Locomotive and Car Research Institute, China Academy of Railway Sciences Company Ltd., Beijing, China. His main research interests include design, modeling and control of bearingless switched reluctance motor.

Xilian Wang received the B.S. and M.S. degrees in electrical engineering from Harbin University of Science and Technology, Harbin, China, in 1997 and 2000, respectively, and the Ph.D. degree in electrical engineering from Beijing Jiaotong University, Beijing, China in 2013.

In 2009, she was an Associate Professor with the School of Electrical Engineering, Beijing Jiaotong University, Beijing, China, where she has been a Professor since 2014. Her current research interests includes areas of motor and electrical appliances, power electronics and power transmission, electrical engineering and rail transit transportation.

Xuan Wang received the B.S. degree in electrical engineering in 2021 from Beijing Jiaotong University, Beijing, China, where she is currently working toward the M.S. degree in electrical engineering with Electrical Engineering College.

Her main research interests include power electronic and control of bearingless switched reluctance motor.

Wenmei Hao received the B.Sc. and Ph.D. degrees in electrical engineering from Beijing Jiaotong University, Beijing, China, in 2016 and 2022, respectively.

From 2019 to 2021, she was with, as a visiting Ph.D. with Politecnico di Torino, Torino, Italy. She is currently a Postdoctor with National Engineering Research Center for Electric Vehicles and School of Mechanical Engineering, Beijing Institute of Technology, Beijing, China. Her current research interests include wireless charging technology and power electronics.

Yan Su received the B.Eng. degree in electrical engineering in 2021 from Beijing Jiaotong University, Beijing, China, where she is currently working toward the master's degree in power electronics and power transmission.

Her research interests include ultrahigh speed brushless dc motor and its control system.

Ruikang Yang received the B.S. degree in electrical engineering in 2022 from Beijing Jiaotong University, Beijing, China, where he is currently working toward the Ph.D. degree in electrical engineering with the School of Electrical Engineering.

His research interest includes control strategy of switched reluctance motor.